npj | precision oncology

Article

Published in partnership with The Hormel Institute, University of Minnesota

https://doi.org/10.1038/s41698-026-01359-4

AI-enabled single-cell dissection of the palmitoylation landscape identifies a multicellular prognostic program in gastric cancer

Check for updates

Jun Xu[1,9], You Hu[2,9], Qiao Qiao[3,9], Yongda Lu[1], Fan Cen[4], Shuoshuo Hou[5], Hongbao Yang[6], Jian Lv[7] ✉, Yan Qin[8] ✉ & Suhua Xia[4] ✉

Gastric cancer remains highly lethal, yet how protein S-palmitoylation shapes tumour ecosystems and clinical outcome is unclear. We integrated single-cell RNA sequencing (119,931 cells from 25 gastric tumours) with spatial transcriptomics and bulk cohorts to delineate palmitoylation-linked states across malignant, immune, and stromal compartments. A palmitoylation-high malignant programme partitioned into three metastasis-enriched subclusters with increased fatty-acid metabolism and Ras–MAPK signalling and predicted worse survival. Spatial mapping and ligand–receptor inference revealed co-localised niches where palmitoylation-high tumour cells interacted with immunosuppressive myeloid cells and distinct CAF subsets, with strengthened pro-angiogenic and pro-fibrotic cues. We derived and validated an 87-gene multicellular palmitoylation signature for risk stratification, and higher scores were consistently associated with adverse outcomes in external cohorts. Drug-response modelling highlighted vulnerabilities involving the HSP90–PI3K/MAPK axis. Functional assays and xenografts confirmed SH3BGRL as a key driver within this poor-prognosis programme.

Gastric cancer (GC) is one of the leading digestive malignancies worldwide in terms of both incidence and mortality[1–3]. Marked by high inter-tumour heterogeneity, late clinical presentation and limited therapeutic options, advanced-stage GC carries a poor prognosis[4–6]. This pronounced heterogeneity complicates patient stratification, contributes to variable treatment responses, and remains a major barrier to durable therapeutic benefit. Over the past decade the tumour immune microenvironment (TIME) has emerged as a critical driver of GC progression, metastasis and treatment resistance[7,8]. The TIME is a multicellular ecosystem composed of immune cells, such as T and B lymphocytes, myeloid subsets, and stromal elements, including cancer-associated fibroblasts, CAFs, and vascular endothelial cells[9–11]. Through intricate intercellular communication networks these compartments orchestrate immune evasion, angiogenesis and metastasis[12,13]. Among them, myeloid cells—tumour-associated macrophages and myeloid-derived suppressor cells (MDSCs)—are central architects of immunosuppression, whereas CAFs and endothelial cells indirectly shape immune cell infiltration and function by remodelling the extracellular matrix and sustaining neovascularisation[14–16].

Protein S-palmitoylation is a reversible lipid modification catalysed by the DHHC family of acyl-transferases[17–19]. By modulating membrane anchoring, stability and protein–protein interactions, palmitoylation has been implicated in the pathogenesis of multiple tumours[20–22]. In GC, palmitoylation of key immune regulators has been shown to tip the balance towards immune escape and chemo-resistance[23,24]. ZDHHC3-mediated palmitoylation of PD-L1 prolongs its half-life, blunts CD8 + T-cell cytotoxicity and predicts poor response to chemotherapy; palmitoylation of the

[1]Department of Gastroenterology, The First Affiliated Hospital of Soochow University, Suzhou, China. [2]Department of General Surgery, The First Affiliated Hospital of Soochow University, Suzhou, China. [3]Department of Digestive Medicine, Affiliated Hospital of Jiangnan University, Wuxi, China. [4]Department of Oncology, The First Affiliated Hospital of Soochow University, Suzhou, China. [5]Animal Experimental Center of the Public Platform, China Pharmaceutical University, Nanjing, China. [6]Department of Basic Medicine, School of Basic Medicine and Clinical Pharmacy, China Pharmaceutical University, Nanjing, China. [7]Department of Thoracic Surgery, Changzheng Hospital, Naval Medical University, Shanghai, Shanghai, China. [8]Department of Pathology, Affiliated Hospital of Jiangnan University, Wuxi, China. [9]These authors contributed equally: Jun Xu, You Hu, Qiao Qiao. ✉e-mail: bluefox811009@163.com; qyqinyan1982@163.com; xiasuhua@suda.edu.cn

The Hormel Institute
University of Minnesota

transcription factors (TF) T-bet and Nrf2 skews Th1 polarisation and antioxidant programmes[25]. Collectively, these observations suggest that palmitoylation rewires the TIME and may serve as a tractable prognostic and therapeutic node.

Single-cell RNA sequencing (scRNA-seq) now allows the heterogeneity and spatial architecture of the TIME to be resolved at single-cell resolution[26–28]. Recent GC atlases have delineated clonal tumour evolution, exhausted T-cell states, CAF and endothelial subtypes, and functionally suppressive monocyte-like MDSCs that correlate with adverse outcomes[29,30]. Nevertheless, a comprehensive, multicompartment atlas that links palmitoylation-associated programmes to lineage-specific states, spatial niches and intercellular communication, and connects these features to patient outcome, is still lacking[31,32].

To address this gap, we integrated single-cell and spatial transcriptomics with bulk transcriptomes and complementary multi-omic layers, and applied machine-learning-based integration to map palmitoylation-associated programmes across malignant, immune and stromal compartments, define cell-type-specific dynamics and communication circuits, and derive an interpretable PAG-based prognostic signature for personalised risk stratification.

Results

Single-cell transcriptomics links epithelial palmitoylation to gastric-cancer metastasis

Single-cell mapping reveals palmitoylation-high (P-high) malignant epithelial cells that are enriched in metastatic gastric tumours. We used UMAP to embed the transcriptomes of 119,931 gastric-tumour cells and, with canonical markers, resolved eight major compartments: epithelial, fibroblast, endothelial, T/NK, B, plasma, myeloid and mast cells (Fig. 1A–C). InferCNV and CopyKAT separated malignant from benign epithelia (Fig. 1D) and the malignant pool was further split into metastatic vs non-metastatic subsets to visualise their spatial segregation (Fig. 1E). Bar plots of cell fractions, counts and mRNA totals confirmed data quality (Fig. 1F–H). Next, CHPF assigned a palmitoylation score to every cell; at the cut-off >2.5 the P-high and palmitoylation-low (P-low) populations formed discrete UMAP clouds (Fig. 1I). These cells were markedly enriched among malignant epithelia (Fig. 1J). A Sankey diagram links cell type, metastatic status and palmitoylation state, implicating the lipid modification in metastatic potential (Fig. 1K). Together, these data indicate that palmitoylation-high malignant epithelial states are over-represented in metastatic gastric tumours.

Palmitoylation-dependent sub-clusters rewire fatty-acid and Ras-MAPK programmes to gastric-tumour metastasis

Re-clustering of malignant epithelium identifies palmitoylation-dependent subclusters that preferentially engage fatty-acid metabolism and Ras-MAPK signalling in metastasis. Malignant epithelia were dichotomised by CHPF score and re-clustered separately. P-high cells resolved into three sub-clusters (P1–P6), P-low into six (N1–N6) (Fig. 2A, B); Bar plots confirmed the split and showed that 5.7% of malignant epithelial cells were P-high in metastatic tumours, compared with 3.2% in non-metastatic tumours (absolute difference +2.5 percentage points; ~1.8-fold enrichment) (Fig. 2C). A heat-map of 1,847 sub-cluster-specific markers revealed P1 enriched for fatty-acid metabolism, P2 for membrane-anchoring and synaptic genes, and P3 for EMT signatures, whereas N1–N6 were dominated by cell-cycle and oxidative-phosphorylation genes (Fig. 2D). WGCNA identified blue, turquoise and yellow modules whose eigengenes correlated strongly with these cells fraction (r = 0.78, 0.71, 0.65) and contained core palmitoylation regulators (ZDHHC5/9, ABHD17B, RAB27A) (Fig. 2E). GO-BP and KEGG enrichment pointed to protein palmitoylation, synaptic-vesicle assembly, ECM adhesion, Ras-MAPK signalling and fatty-acid metabolism—suggesting that palmitoylation drives metastasis by remodelling membrane micro-domains and activating the Ras-MAPK axis (Fig. 2F–K). Thus, palmitoylation-high subclusters are associated with fatty-acid–Ras/MAPK programmes that are linked to gastric-tumour metastasis.

Palmitoylation-high tumour cells adopt an AP-1/TEAD4-driven, high-invasion/high-apoptosis programme that bypasses canonical EMT

P-high tumour cells exhibit a non-canonical phenotype characterised by high invasion and apoptosis despite low canonical EMT activity. Using CancerSEA gene sets we calculated single-cell GSVA scores for apoptosis, invasion, EMT and stemness. Palmitoylation score correlated positively with apoptosis ($R = 0.39$, $p < 0.001$) and invasion ($R = 0.27$, $p < 0.001$) but negatively with EMT ($R = -0.27$, $p < 0.001$) (Fig. 3A). P-high clusters (P1–P3) displayed high apoptosis and invasion yet low EMT, indicating a non-canonical, high-invasion/high-apoptosis phenotype (Fig. 3B). SCENIC network analysis contrasting P1–P3 with the least-invasive N3 cluster identified FOSL1, JUNB, STAT3 and TEAD4 as hub TFs (top 1% degree) (Fig. 3C, D). Correlation with Hallmark pathways ($|r| > 0.2$, $p < 0.05$) showed FOSL1/JUNB co-activated with NF-κB-apoptosis and hypoxia signatures, whereas TEAD4 aligned with PI3K-AKT-mTOR, implying that an AP-1/TEAD4 axis sustains invasion while bypassing classical EMT (Fig. 3E). Collectively, an AP-1/TEAD4-centred regulon underpins a non-canonical, invasive yet apoptosis-prone phenotype in palmitoylation-high tumour cells.

A 21-gene P-high signature from ridge regression predicts poor overall survival across 1239 gastric-cancer patients

A ridge-derived P-high transcriptional signature robustly stratifies overall survival across multicohort gastric-cancer datasets. Univariate Cox regression in the GEO training set ($n = 867$) yielded 87 survival-linked, P-high-specific genes. 101 machine-learning pipelines were benchmarked; Ridge regression ($\lambda = 0.032$) achieved the highest cross-validated C-index (0.742) and was selected (Supplementary Fig. 1A). The optimal cut-off (risk score = 1.34) stratified patients into high- and low-risk groups. Five-year OS was 38 vs 71% in the training set ($p < 0.0001$), indicating a 33-percentage-point absolute decrease (~1.9-fold lower 5-year survival probability) in high-risk patients; a similar pattern was observed in the independent GEO_Test cohort (42 vs 65%; 23-point decrease, ~1.5-fold lower; $p = 0.079$). In the merged GEO set ($n = 1239$) high-risk patients had a 2.18-fold death hazard ($p < 0.0001$), and the signature remained prognostic in the external TCGA-STAD cohort (35 vs 63%; 28-point decrease, ~1.8-fold lower; $p = 0.00011$) (Supplementary Fig. 1B–E). In summary, the palmitoylation-high transcriptional signature provides reproducible risk stratification across independent gastric-cancer cohorts.

High-risk P-high tumours harbour KRAS/TP53 co-alterations, global hypomethylation and an EGFR-AKT-STAT3 phosphorylation cascade

Multi-omic profiling links the high-risk P-high group to KRAS/TP53 alterations, global hypomethylation, and activated EGFR-AKT-STAT3 signalling. Whole-exome data revealed higher frequencies of TP53, KRAS G12C and KEAP1 mutations, MDM2/MYC amplifications and CDKN2A deletions in the high-risk group (Supplementary Fig. 2A). Broad-level CNVs showed gains of 1q, 3q, 5p and losses of 9p21.3 and 17p13.1; focal amplifications targeted CDK4, CCND1 and EGFR (Supplementary Fig. 2B). TMB was almost doubled in high-risk tumours (12.4 vs 6.1 mutations/Mb, $p = 0.000059$) and correlated with risk score (Supplementary Fig. 2C). Methylation arrays uncovered global hypomethylation; promoter methylation of YTHDF2 was reduced ($\beta = 0.21$ vs 0.48, $p = 0.0000016$), matching its elevated expression and suggesting m^6A-driven stabilisation of oncogenic transcripts (Supplementary Fig. 2D). Proteomics confirmed higher phosphorylation of EGFR, AKT and STAT3 in high-risk samples, supporting a palmitoylation-membrane-localisation-phosphorylation cascade (Supplementary Fig. 2E). Overall, high-risk tumours show coordinated genomic, epigenetic and

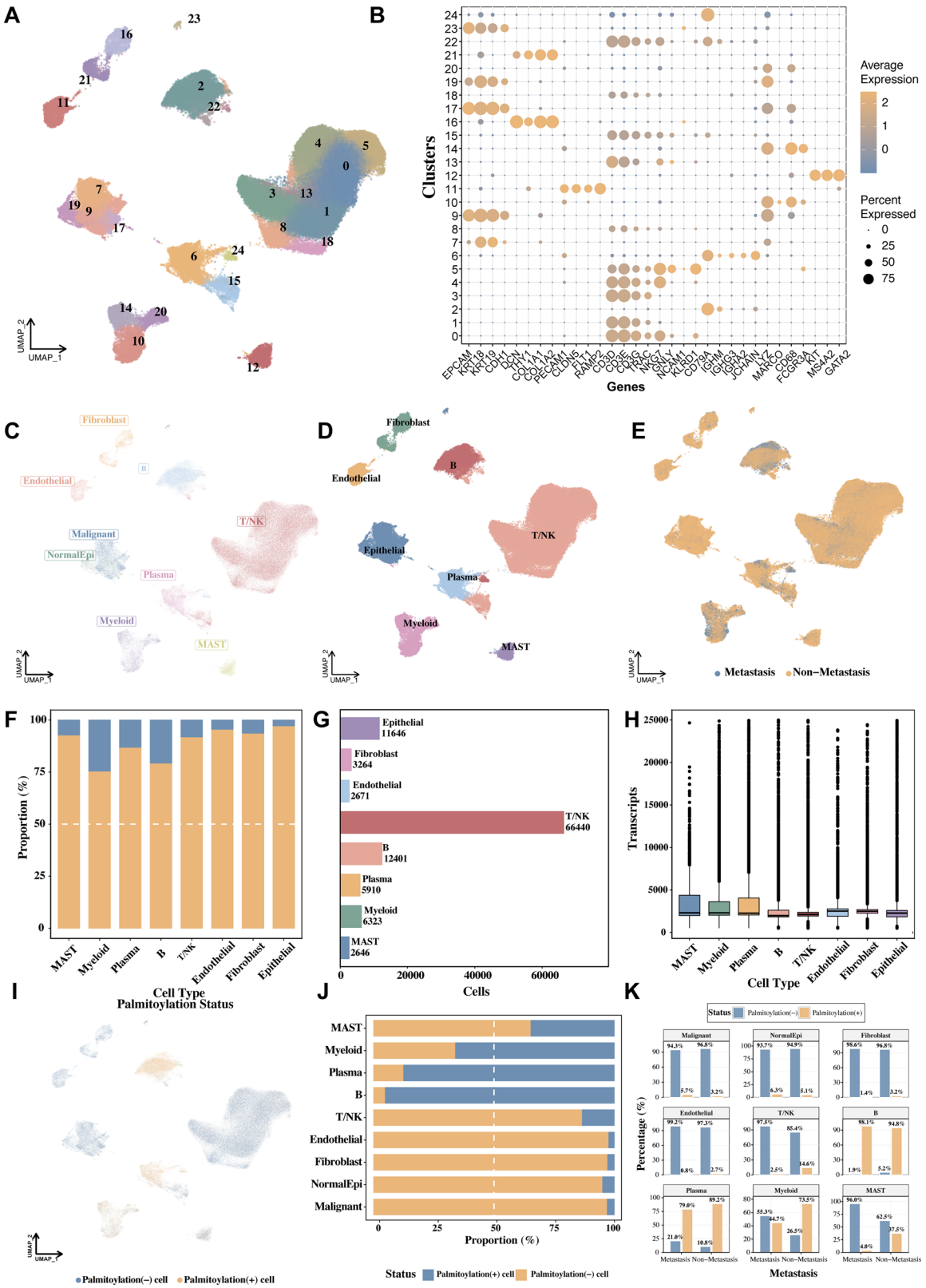

Fig. 1 | Single-cell atlas of GC. A UMAP plot of single-cell data coloured by clustering clusters. **B** Bubble plot showing the expression of canonical cell markers across different clusters. **C–E** UMAP plots of single-cell data showing cell types, malignant cells (after identification), and presence/absence of distant tumour metastasis. **F–H** Statistical plots showing the proportion of cells with/without distant tumour metastasis, cell count, and transcript number for each cell type. **I** UMAP plot distinguishing palmitoylated vs. non-palmitoylated cells identified by CHPF software. **J** Bar chart showing the proportion of palmitoylated vs. non-palmitoylated cells in each cell type. **K** Sankey diagram illustrating the associations between cell type, sample type, and palmitoylation status.

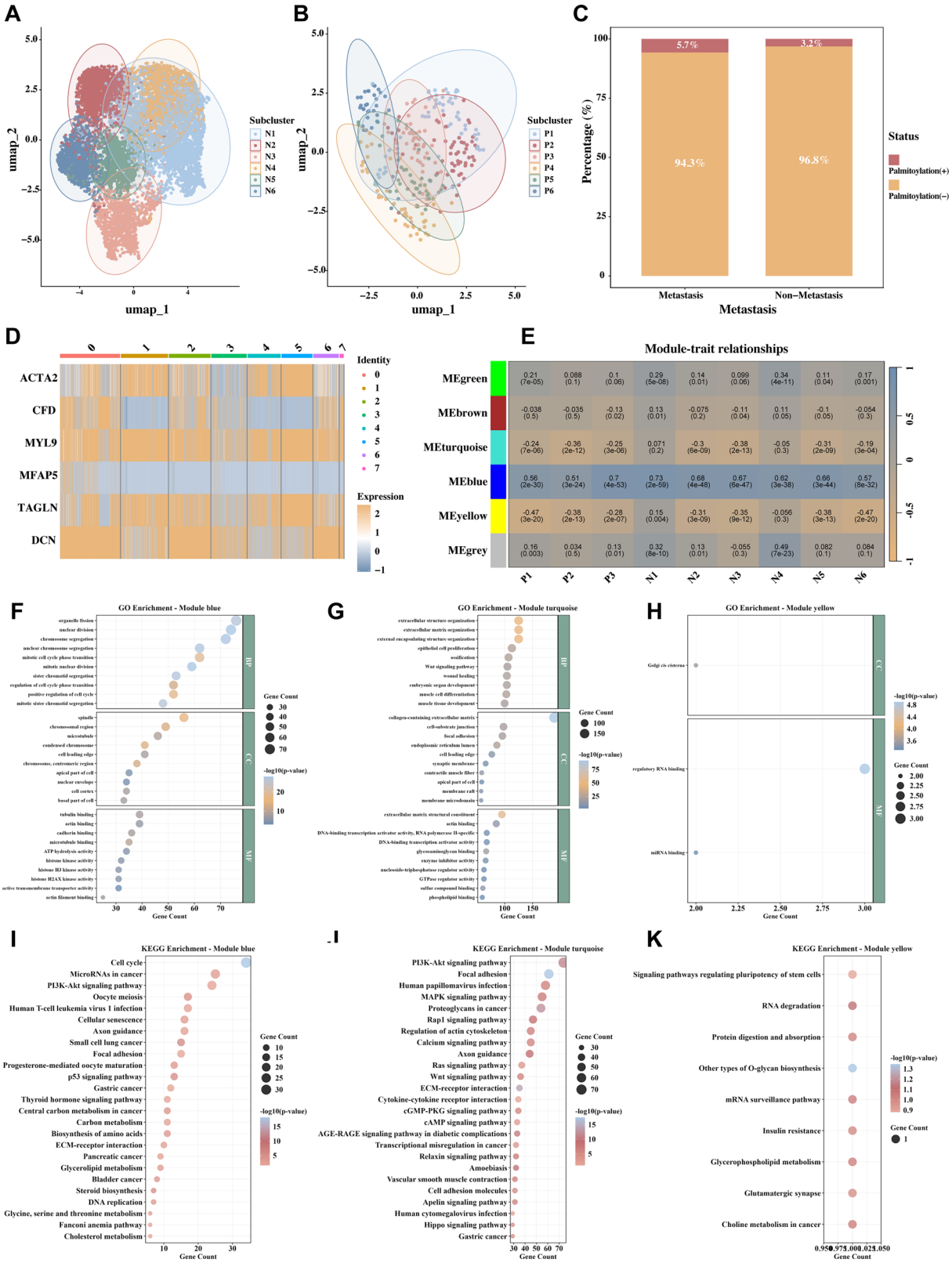

Fig. 2 | Analysis results of tumour cell subsets. A–C UMAP plots of palmitoylated and non-palmitoylated cell populations; Sankey diagram showing the proportion of cells with/without distant tumour metastasis and palmitoylation status; and ridge-line plot of palmitoylation scores for each cell population. **D** Heatmap of marker gene expression across different cell populations. **E** Heatmap showing the correlation between gene modules (from WGCNA analysis) and each cell population. **F–K** Results of GO-Biological Process (GO-BP) and KEGG enrichment analyses for the blue, turquoise, and yellow gene modules.

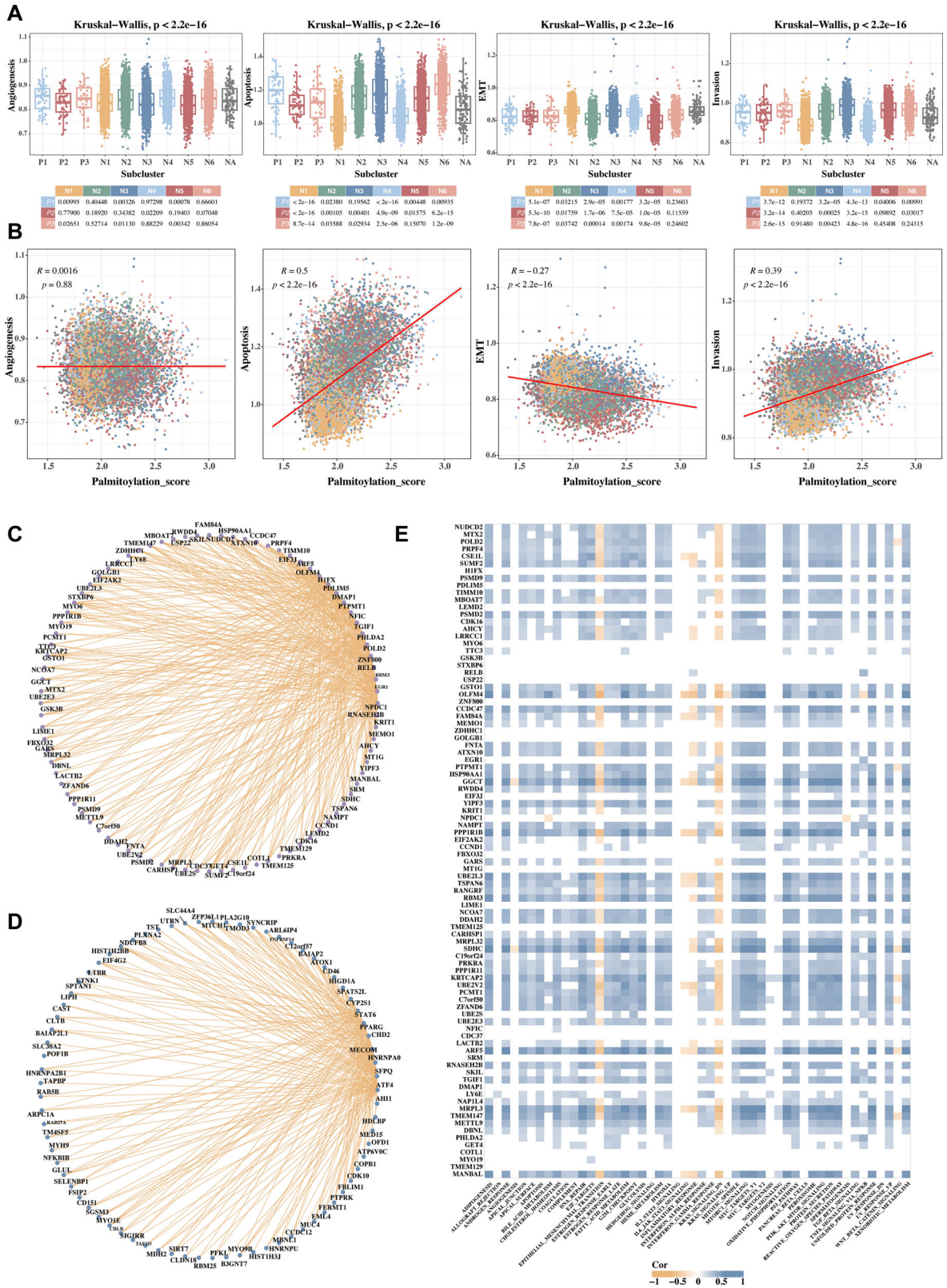

Fig. 3 | Analysis results of tumour-related pathways, CNVs, and transcription factors (TFs). A Scatter plots showing the correlation between palmitoylation scores and scores of four signatures. **B** Box plots showing the differences in scores of the four signatures across different cell populations. **C**, **D** Network diagram of the top 1% TFs in palmitoylated (P) cells and the N3 (non-palmitoylated) cell population. **E** Heatmap showing the correlation between TFs/genes unique to the P group and Hallmark pathways (only correlations with |Cor | > 0.2 and $p < 0.05$ are shown).

phosphoproteomic activation consistent with EGFR–AKT–STAT3 signalling.

CDC37-HSP90–PI3K/MAPK axis emerges as top druggable vulnerability of P-high gastric-tumour cells

In silico vulnerability mapping nominates the CDC37-HSP90-PI3K/MAPK axis as a therapeutically actionable dependency of P-high tumour cells. The 312 genes uniquely up-regulated in P-high cells were correlated with 265 compounds in GDSC. Celastrol (CDC37 inhibitor), luminespib (HSP90), dactolisib (PI3K/mTOR), trametinib (MEK) and TVB-2640 (FASN inhibitor) showed the strongest associations ($|r| > 0.3$, $p < 0.05$) (Fig. 4A). Target-pathway mapping highlighted CDC37-HSP90 client folding, PI3K-AKT-mTOR, Ras-MAPK and fatty-acid synthesis (Fig. 4B). A CDC37-centred network illustrated its bottleneck position (Fig. 4E). CMap queries using P-high genes as "up" and N3 genes as "down" tags returned 17-AAG, luminespib, GDC-0941, selumetinib and fasnall (Score > 90, FDR < 0.01) (Fig. 4C, D, F). Thus, the CDC37-HSP90 axis and its downstream PI3K/MAPK branches represent actionable vulnerabilities of P-high tumour cells. Together, these results highlights the CDC37–HSP90 and PI3K/MAPK pathways as tractable vulnerabilities of the palmitoylation-high state.

P-high M2 macrophages and pDC mark an immunosuppressive, hypoxia-linked axis that doubles gastric-cancer death risk

To understand how palmitoylation shapes the tumour microenvironment, we profiled myeloid subsets and found that P-high M2 macrophages and pDCs define an immunosuppressive, hypoxia-associated state linked to worse survival. Re-clustering of 28,432 myeloid cells yielded classical mono, non-classical mono, M1/M2 macrophages, mDC, pDC and mast cells (Fig. 5A, B). P-high fractions were highest in M2 macrophages and pDC (~42%) and lowest in classical monocytes (~15%), corresponding to an approximate 2.8-fold enrichment of P-high states in M2/pDC subsets relative to classical monocytes, based on 28,432 myeloid cells analysed (Figs. 5E, F, 4H). Sankey and UMAP plots traced a dominant "M2-pDC- P-high -metastasis" trajectory and co-localisation with hypoxia signatures (Fig. 5C, D, G, I). BisqueRNA deconvolution of TCGA-STAD showed that every 10% increase in M2 P-high proportion raised death risk by 88% (HR = 1.88, $p = 0.002$), corresponding to an ~1.9-fold increase in instantaneous mortality risk. Notably, this association remained significant in multivariable Cox models adjusting for age and AJCC pathological stage (with additional adjustment for chemotherapy/radiotherapy where available in TCGA clinical annotations), whereas high classical-mono P-low content was protective (HR = 0.52, $p = 0.04$) (Fig. 5J). Thus, palmitoylation-high myeloid states couple hypoxia-associated immunosuppression with increased mortality risk.

SPP1–CD44, GAS6–AXL and LGALS9–HAVCR2 immunosuppressive circuits spatially co-localise with palmitoylation-high tumour cores

Cell-cell communication and spatial mapping pinpoint P-high immunosuppressive circuits, led by SPP1-CD44, that concentrate within hypoxic tumour cores. ROGUE indices (>0.92 for M2 and pDC) ensured purity prior to CellChat. These myeloid cells engaging P-high epithelia displayed the strongest SPP1-CD44, GAS6-AXL and LGALS9-HAVCR2 immunosuppressive axes, whereas double-negative pairs favoured MIF-(CD74 + CXCR4) and ANXA1-FPR1 pro-inflammatory circuits (Fig. 6A–C, E). Spatial transcriptomics co-mapped SPP1 and CD44 to hypoxic tumour cores where palmitoylation scores were highest, validating SPP1-CD44 as a spatially confined, hypoxia-driven feed-forward loop (Fig. 6D, F). Taken together, spatially co-localised SPP1–CD44 and related axes support a hypoxia-driven, immunosuppressive feed-forward loop. Here, "hypoxia-driven" is used in the spatial/transcriptomic sense (enrichment of P-high states in hypoxia-high regions and positive correlation with hypoxia signatures), and does not by itself prove that hypoxia directly induces palmitoylation enzymes (e.g., ZDHHC family).

P-high myCAF and iCAF populate hypoxic niches and portend 2.3-fold higher death risk in GC

To extend our analysis to stromal remodelling, we examined fibroblast subsets and found that P-high myCAFs and iCAFs accumulate in hypoxic niches and independently associate with increased mortality risk. Re-clustering of 18,000 fibroblasts identified NF, myCAF, iCAF, apCAF and adipoCAF subsets (Supplementary Fig. 3A, B). P-high cells were concentrated in myCAF and iCAF (~39% and 35%), representing ~3.3-fold and ~2.9-fold enrichment relative to NF (~12%), based on the fibroblast subset analysed (Supplementary Fig. 3E, H, I). A Sankey trace revealed a "myCAF-P-high-metastasis" axis; UMAP showed P-high fibroblasts localised to hypoxic niches ($R = 0.41$, $p < 0.001$) (Supplementary Fig. 3C, D, F, G). BisqueRNA deconvolution indicated that a 10% increment in myCAF P-high fraction increased death hazard 2.3-fold (HR = 2.30, $p = 0.003$), and this effect estimate was robust to multivariable adjustment for age and AJCC pathological stage (and for chemotherapy/radiotherapy when available in TCGA). By contrast, high NF P-low content was favourable (HR = 0.31, $p = 0.03$; ~69% lower hazard) (Supplementary Fig. 3J). In summary, palmitoylation-high CAF subsets occupy hypoxic niches and independently predict poorer survival.

MDK–NCL, AREG–ERBB and TGFB1 axes at the hypoxic tumour–stroma interface drive pro-fibrotic invasion by P-high fibroblasts

Ligand-receptor analysis implicates MDK-NCL, AREG-ERBB and TGFB1 signalling at the tumour-stroma interface as key mediators of P-high fibroblast-driven invasion. High-purity myCAF and pericyte clusters (ROGUE > 0.93) were used for CellChat. P-high fibroblasts engaging P-high epithelia showed strongest MDK-NCL, AREG-(EGFR + ERBB2), TGFB1-(TGFBR1 + TGFBR2) and SEMA3C-(NRP1 + PLXNA1) pro-fibrotic/invasion signals, whereas double-negative pairs favoured BMP and PROS1-AXL anti-inflammatory circuits (Supplementary Fig. 4A–D). Spatial maps co-localised MDK and NCL at the tumour-stromal interface under hypoxic conditions (overlap coefficient 0.76), identifying MDK-NCL as a hypoxia-driven paracrine axis (Supplementary Fig. 4E, F). Thus, MDK–NCL, AREG–ERBB and TGFB1 signalling likely mediates fibroblast-driven invasion in the palmitoylation-high microenvironment.

P-high tumour EC and tip EC align with VEGFA-high niches and confer a 2.8-fold mortality increase

Finally, to assess vascular remodelling in the palmitoylation-high microenvironment, we analysed endothelial subsets and found that P-high tumour EC and tip EC populations align with VEGFA-high regions and adverse outcome. Re-clustering of 9000 endothelial cells yielded arterial, venous, lymphatic, tumour EC and tip EC subsets (Supplementary Fig. 5A, B). P-high fractions peaked in tumour EC and tip EC (~41 and 38%) and were lowest in lymphatics (~13%), corresponding to ~3.2-fold and ~2.9-fold enrichment compared with lymphatic endothelium, based on the endothelial subset analysed (Supplementary Fig. 5E-F, 5H). A Sankey diagram traced a "tumour EC-tip EC-P-high-metastasis" flow; UMAP showed these endothelial cells aligned with VEGFA-high regions ($R = 0.44$, $p < 0.001$) (Supplementary Fig. 5C, D, G, I). BisqueRNA deconvolution showed that each 10% increase in the tumour EC P-high proportion was associated with a 2.8-fold higher death hazard (HR = 2.81, $p = 0.01$). Importantly, this association remained statistically significant after multivariable correction for age and AJCC pathological stage (and additionally for chemotherapy/radiotherapy when available in TCGA), whereas lymphatic P-low content was protective (HR = 0.47, $p = 0.04$) (Supplementary Fig. 5J). Collectively, palmitoylation-high endothelial programmes align with VEGFA-rich niches and associate with adverse clinical outcome.

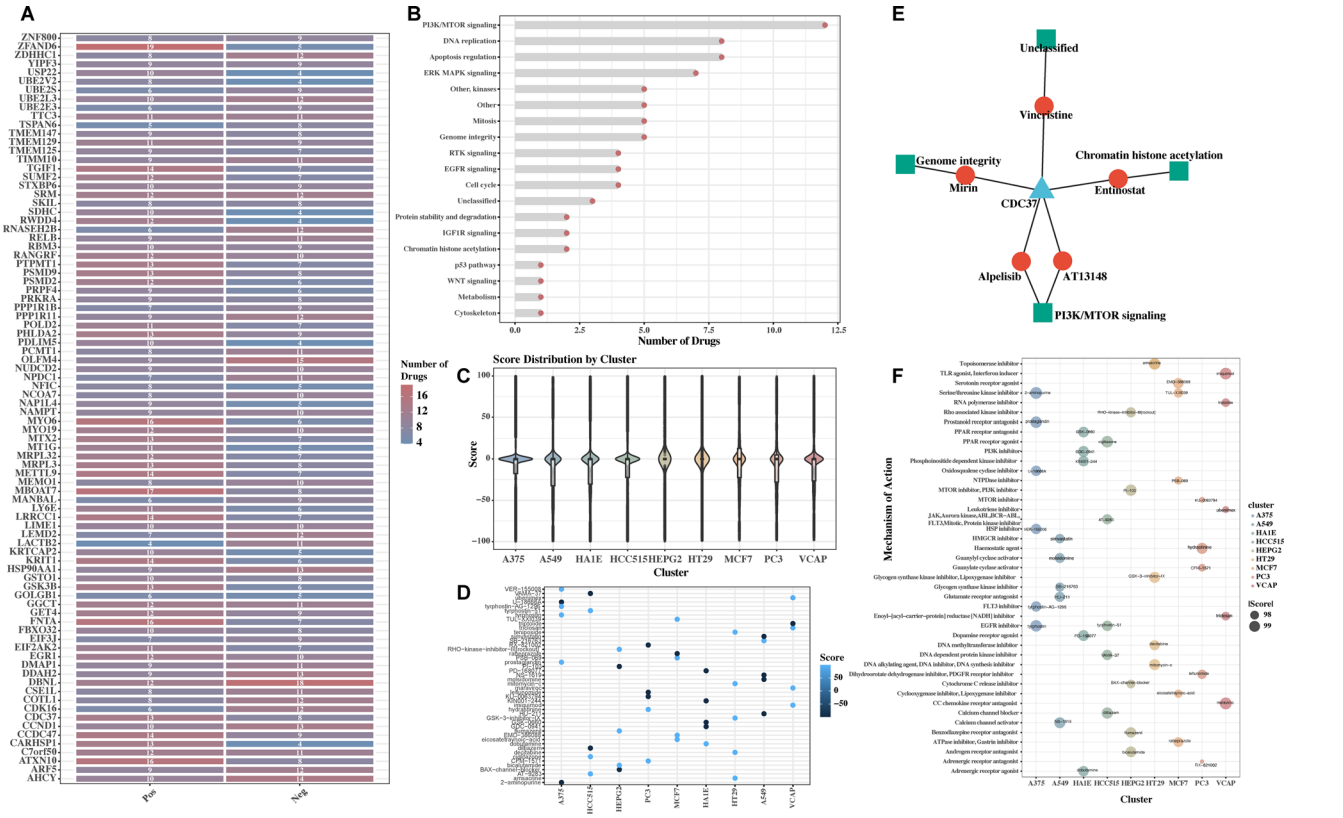

Fig. 4 | Drug analysis results. A Bar chart showing the statistical significance of correlations between TFs/genes unique to the P group and drugs. **B** Bar chart showing the statistical distribution of target pathways associated with the drugs. **C** Results of CMap online analysis: Violin plot showing compound scores across different cell lines. **D** Bubble plot summarising the top five compounds (by |Score|) in each cell line. **E** Network diagram of the model gene CDC37, its associated drugs, and their target pathways. **F** Bubble plot summarising the target pathways of the top five compounds (by |Score|) in each cell line.

LGALS9–CD44, VEGFA–VEGFR and WNT5B axes from hypoxic P-high endothelium are linked to angiogenic and invasive niches

P-high endothelium engages tumour cells through pro-angiogenic LGALS9-CD44 and VEGFA-VEGFR signalling, reinforcing invasive vascular niches. Tip and arterial EC clusters (ROGUE > 0.94) were compared by CellChat. These cells endothelium engaging P-high epithelia exhibited strongest LGALS9-CD44, VEGFA-VEGFR1/2, MDK-NCL, WNT5B-FZD4/6 and SEMA3C-(NRP1 + PLXNA2) pro-angiogenic/invasion axes, whereas double-negative pairs favoured CXCL-ACKR1 and ADM-CALCRL homing pathways (Supplementary Fig. 6A–D). Spatial transcriptomics co-mapped LGALS9 and CD44 around hypoxic tumour vessels (overlap coefficient 0.79), confirming LGALS9-CD44 as a spatially resolved, hypoxia-driven paracrine relay (Supplementary Fig. 6E, F). Together, palmitoylation-high endothelium reinforces angiogenic and invasive niches through VEGFA–VEGFR and LGALS9–CD44 signalling.

The protein SH3BGRL is a novel prognostic driver of gastric-cancer progression

Functional experiments validate SH3BGRL as a driver of gastric-cancer proliferation, invasion and tumour growth in vivo. Having identified SH3BGRL as a key component of a poor-prognosis signature, we investigated its functional role in GC. Interrogation of TCGA data revealed that SH3BGRL expression was significantly elevated in tumour tissues compared to adjacent normal mucosa (Supplementary Fig. 7A). Consistent with its pro-tumourigenic potential, high SH3BGRL expression correlated strongly with poor overall survival in patients (Supplementary Fig. 7B). We next quantified SH3BGRL mRNA levels across a panel of GC cell lines (AGS, BGC823, NCI-N87, HGC-27) and the immortalised gastric mucosal cell line GES-1. SH3BGRL was broadly upregulated in GC lines, with BGC823 showing the highest and AGS the lowest expression (Supplementary Fig. 7C). We therefore engineered loss-of-function and gain-of-function models by knocking down SH3BGRL in BGC823 cells and overexpressing it in AGS cells, respectively, with efficiency confirmed by qRT–PCR (Fig. 7A). Functional assays demonstrated that SH3BGRL is a potent regulator of GC cell malignancy. SH3BGRL knockdown markedly attenuated, whereas its overexpression enhanced, cellular proliferation (CCK-8 assay, Fig. 7B) and clonogenic survival (Fig. 7C). Furthermore, silencing SH3BGRL promoted apoptosis, while its overexpression exerted a protective effect against cell death (Fig. 7D). The pro-metastatic function of SH3BGRL was confirmed by transwell assays, which showed that its depletion crippled, and its overexpression fortified, the invasive and migratory capacities of GC cells (Fig. 7E). At the molecular level, modulation of SH3BGRL reciprocally regulated epithelial–mesenchymal transition (EMT) markers: knockdown increased E-cadherin and decreased Vimentin, whereas overexpression produced the opposite effect (Fig. 7F). The tumour-promoting role of SH3BGRL was validated in vivo. Subcutaneous xenografts derived from SH3BGRL-knockdown BGC823 cells exhibited significantly slower tumour growth (Fig. 8A, B) and yielded lower final tumour weights compared to controls (Fig. 8C). Immunohistochemical analysis of the xenograft tissues revealed a substantial reduction in Ki-67-positive proliferating cells upon SH3BGRL knockdown (Fig. 8D). Conversely, TUNEL staining showed a significant increase in apoptosis in the SH3BGRL-depleted tumours (Fig. 8E). Taken together, SH3BGRL promotes proliferative, invasive and tumourigenic phenotypes, supporting its role as a functional driver within the poor-prognosis programme.

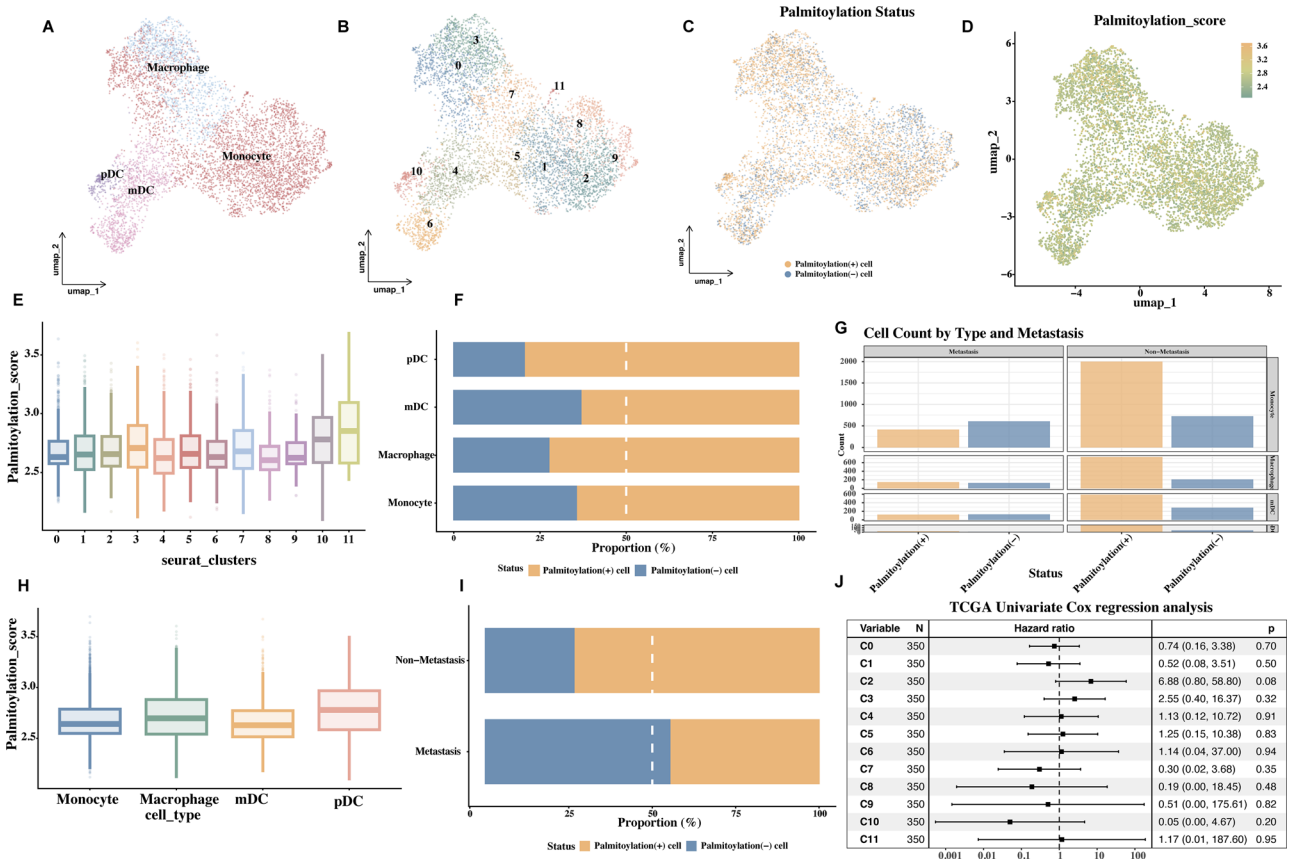

Fig. 5 | Analysis results of myeloid cells. A, **B** UMAP plots of myeloid cells coloured by clustering clusters and cell annotation results. **C**, **D** UMAP visualisation of palmitoylated cells and palmitoylation scores. **E** Box plot of palmitoylation scores across different clusters. **F** Bar chart showing the proportion of palmitoylated vs. non-palmitoylated cells in each myeloid cell type. **G** Sankey diagram illustrating the associations between myeloid cell type, presence/absence of distant tumour metastasis, and palmitoylation status. **H** Box plot of palmitoylation scores for each cell type. **I** Bar chart showing the proportion of palmitoylated vs. non-palmitoylated cells in samples with/without distant tumour metastasis. **J** Forest plot of univariate Cox analysis for the composition of myeloid cell clusters in TCGA bulk data (predicted using the BisqueRNA package).

Discussion

GC remains a clinical challenge whose poor prognosis is driven by late diagnosis, profound inter-tumour heterogeneity and a microenvironment that actively fosters immune evasion, angiogenesis and metastasis[33,34]. Recent single-cell and spatial transcriptomic atlases have delineated malignant lineage states and the tumour microenvironment in GC, providing a high-resolution framework for studying subtype-specific programmes and metastatic dissemination[35]. However, palmitoylation in GC has largely been investigated either through mechanistic studies of individual substrates (for example, PD-L1 palmitoylation) or through bulk-level palmitoylation-related signatures and machine-learning models, leaving unanswered how palmitoylation-associated programmes are organised across cell types and niches in vivo[36–38]. Here, by integrating 119,931 single-cell transcriptomes with complementary bulk and clinical cohorts, we provide, to our knowledge, the first integrative single-cell and multi-omic characterisation of palmitoylation-associated transcriptional programmes across malignant, immune and stromal compartments in GC, and link these programmes to metastatic propensity and patient prognosis.

Palmitoylation is not merely a tumour-cell-intrinsic regulator but a multicellular ecosystem switch[39,40]. Malignant epithelia with high palmitoylation scores segregated into three transcriptionally distinct subclusters (P1–P3) that are enriched for fatty-acid metabolism, synaptic/anchoring genes and EMT programmes, yet paradoxically display a non-canonical "high-invasion/high-apoptosis" phenotype (invasion $R = 0.39$, $p < 0.001$; apoptosis $R = 0.39$, $p < 0.001$; EMT $R = -0.27$, $p < 0.001$). This suggests that palmitoylation enables metastatic fitness through Ras-MAPK-driven membrane plasticity and ECM remodelling rather than through classical EMT, while simultaneously priming cells for apoptosis—potentially reflecting a fitness–liability trade-off. Biochemically, palmitoylation of H- and N-Ras is controlled by an acylation–deacylation cycle that regulates Golgi-to-plasma-membrane trafficking and thereby partitions Ras signalling in space and time[41]. At the plasma membrane, palmitoylated Ras can preferentially associate with cholesterol-rich nanodomains and form signalling nanoclusters, which shape MAPK output and cytoskeleton-coupled membrane remodelling[42]. Moreover, palmitoylation of receptor tails (e.g., EGFR) can modulate adaptor recruitment and endocytic routing, including Grb2 engagement, providing a plausible biochemical basis for enhanced invasion alongside stress sensitivity[43].

This interpretation remains speculative and should be tested in future longitudinal or lineage-tracing studies that can directly quantify turnover within metastatic lesions. From a mechanistic standpoint, this multicellular signal is captured by a transcriptional signature that spans palmitoylation writers (ZDHHC acyltransferases), erasers (depalmitoylases/thioesterases) and downstream palmitoylation-dependent effectors/substrates, supporting that the phenotype we describe reflects dynamic palmitoylation turnover rather than a single enzymatic class.

Taken together, these analyses suggest that palmitoylation-high programmes co-emerge across malignant epithelium and key immune/stromal partners, aligning M2 macrophage/pDC immunosuppression, myCAF-driven fibrotic invasion and endothelial angiogenesis within shared hypoxic niches[44,45]. P-high M2 macrophages and pDCs (~42% of each subset) transmit immunosuppressive SPP1-CD44, GAS6-AXL and LGALS9-

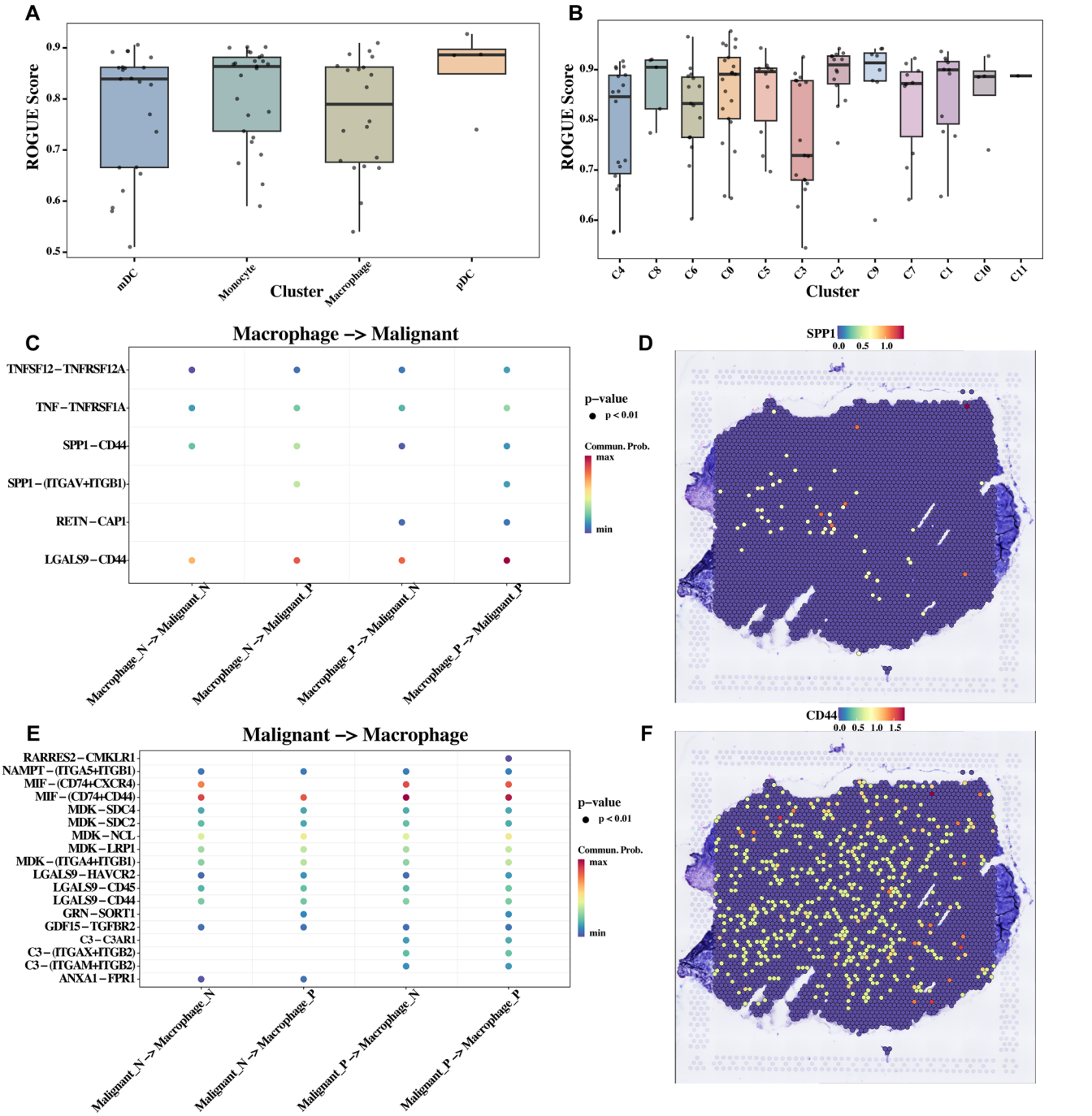

Fig. 6 | Cell communication analysis results of myeloid cells. A, **B** Box plot showing the purity of clusters and cell annotation results (calculated using the ROGUE package for myeloid cells). **C**, **E** Bubble plot of ligand-receptor communication between myeloid cells (palmitoylated vs. non-palmitoylated) and malignant cells (palmitoylated vs. non-palmitoylated). **D**, **F** Expression plot of the ligand-receptor pair (CD44 and SPP1) in spatial transcriptomic data.

HAVCR2 signals to P-high tumour cells, creating a hypoxia-reinforced feed-forward loop that correlates with an 88% increase in death risk for every 10% rise in M2-P-high fraction. Similarly, P-high myCAFs and tumour ECs (39% and 41% P-high, respectively) engage cancer cells via MDK-NCL, AREG-EGFR/ERBB2 and VEGFA-VEGFR axes, doubling or tripling hazard ratios while co-localising with hypoxic niches in spatial maps. Thus, palmitoylation synchronises a multicellular programme that couples immune evasion, fibrotic invasion and pathological angiogenesis.

Importantly, the hypoxia–palmitoylation linkage in our study should be interpreted primarily as an association rather than a proven causal chain. Palmitoylation scores were positively correlated with hypoxia gene-set activity and palmitoylation-high compartments were spatially enriched in hypoxic cores; however, the current datasets do not directly test whether hypoxia transcriptionally upregulates specific palmitoyltransferases (e.g., ZDHHC enzymes) or simply marks the microenvironmental niche where palmitoylation-high states accumulate. Mechanistically, hypoxia/HIF signalling is known to reprogramme lipid uptake and metabolism, which may expand intracellular palmitoyl-CoA availability and thereby facilitate dynamic S-palmitoylation turnover and membrane microdomain signalling[46,47]. Targeted perturbation experiments under controlled oxygen conditions will be needed to disentangle enzyme induction from micro-environmental co-localisation.

Translating this biology into the clinic, we derived an 87-gene P-high signature that achieved a cross-validated C-index of 0.742 and

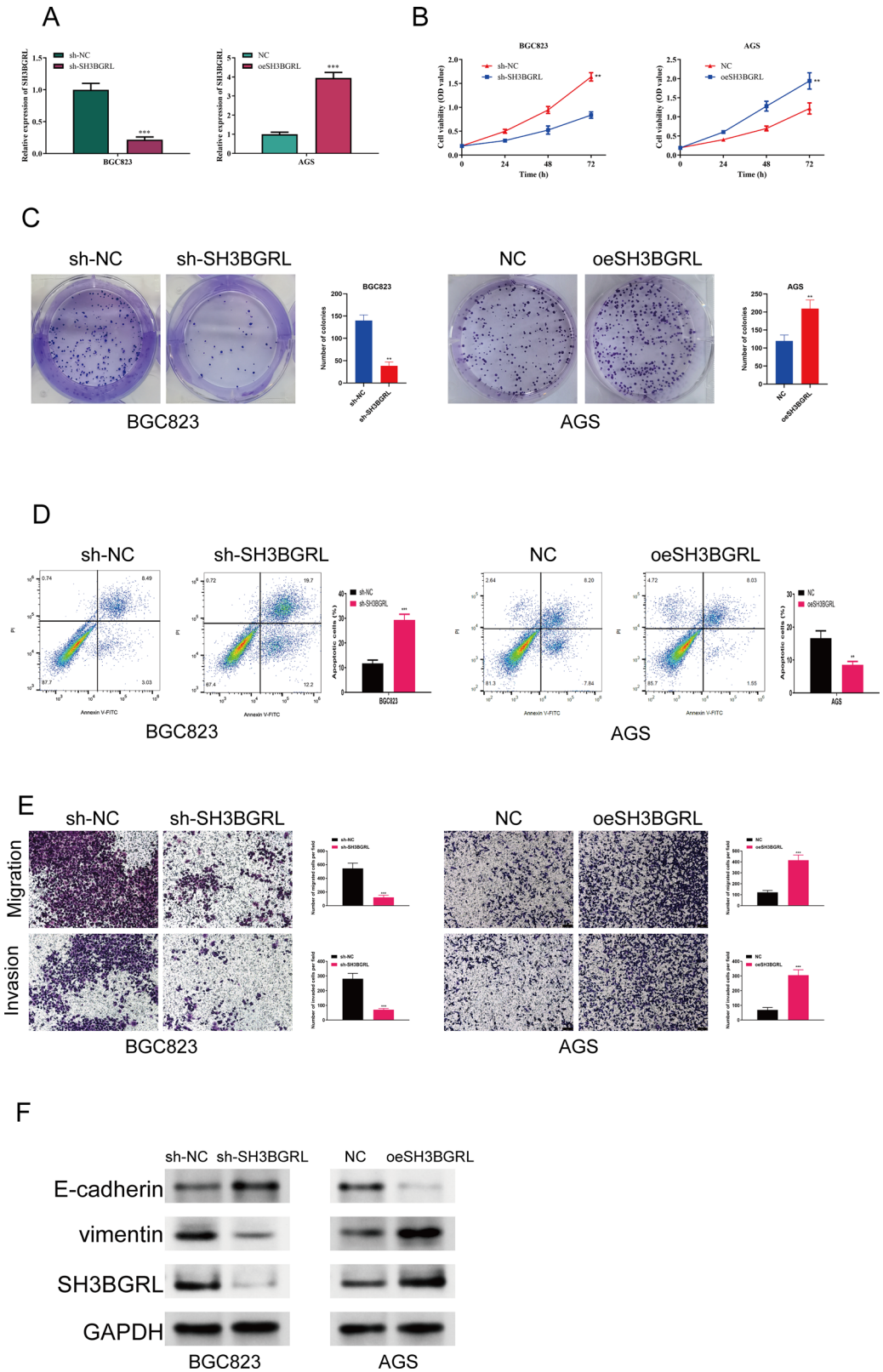

Fig. 7 | SH3BGRL promotes malignant phenotypes of gastric cancer cells in vitro. **A** qRT–PCR validation of SH3BGRL knockdown (KD) in BGC823 cells and overexpression (OE) in AGS cells. **B** Cell proliferation measured by CCK-8 assay at indicated time points in SH3BGRL-modulated cells and their corresponding controls. **C** Representative images and quantification of colony formation assays. **D** Apoptosis analysis by flow cytometry. **E** Representative images and quantification of cell invasion and migration assays performed using Transwell chambers. **F** Western blot analysis of E-cadherin and Vimentin protein expression in SH3BGRL-modulated cells.

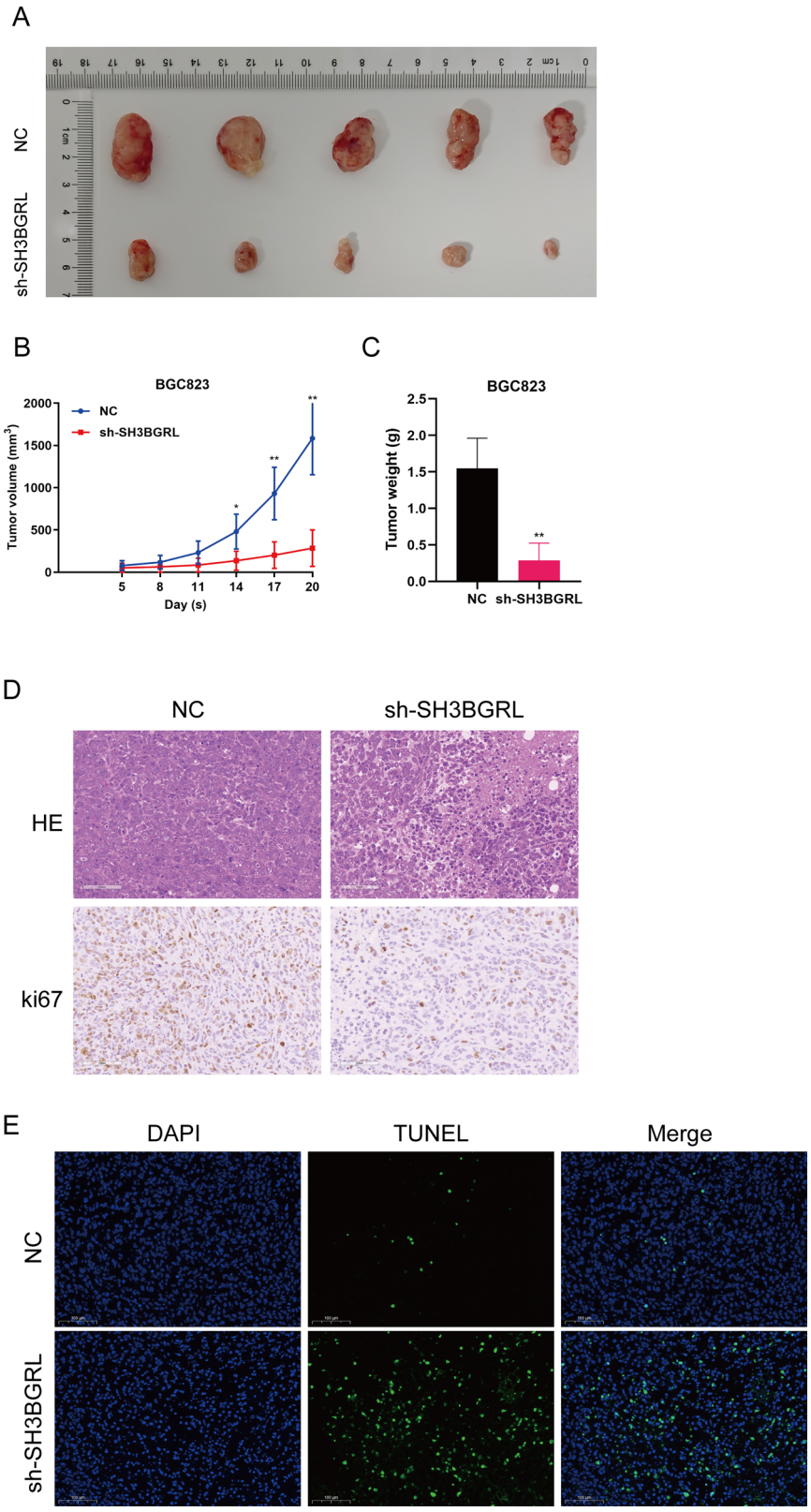

Fig. 8 | SH3BGRL knockdown suppresses tumour growth in vivo. A Representative images of subcutaneous tumours resected from NOD-scid mice at day 20 after injection with BGC823 control or SH3BGRL-knockdown cells. **B** Tumour growth curves measured over 20 days. **C** Tumour weights measured at the end of the experiment. **D** Representative images of immunohistochemical staining for the proliferation marker Ki-67 in xenograft tumour sections. **E** Representative images of TUNEL staining for apoptotic cells in xenograft tumour sections.

stratified 1239 GC patients into high- and low-risk groups with 5-year OS of 38% vs 71% ($p < 0.0001$); performance remained robust in external TCGA-STAD (35 vs 63%, $p = 0.00011$). The signature is independent of stage and grade, and its utility is biologically grounded: high-risk tumours harbour twice the TMB, frequent KRAS-G12C/TP53 mutations, MDM2/MYC amplifications, global hypomethylation and hyper-phosphorylated EGFR-AKT-STAT3—molecular features compatible with addiction to CDC37-HSP90 client folding and PI3K-MAPK signalling. Mechanistically, S-palmitoylation has been reported to stabilise membrane-associated signalling proteins by promoting forward trafficking and retention in lipid microdomains, whereas loss of palmitoylation can cause mislocalisation and increased ubiquitin-

mediated degradation. Such membrane-proximal proteostasis demands are particularly relevant to kinase-driven pathways, because palmitoylated receptors/adaptors and small GTPases scaffold PI3K and MAPK cascades and require proper folding/assembly for sustained signalling. CDC37-HSP90 is a dedicated chaperone system for kinase client maturation and stability; accordingly, our in-silico dependency signal for CDC37-HSP90 provides a plausible proteostatic link between palmitoylation-high programmes and kinase-rich oncogenic networks.

Consistently, in-silico screening and CMap connectivity analyses nominated CDC37 inhibitors (celastrol, 17-AAG), HSP90 blockers (luminespib), PI3K/mTOR and MEK inhibitors (dactolisib, trametinib, selumetinib) and FASN antagonists (TVB-2640, fasnall) as selective vulnerabilities of P-high cells, providing an immediately testable therapeutic roadmap.

From a translational standpoint, our findings support a pragmatic workflow: (i) develop a clinically deployable assay for the P-high programme (e.g., a targeted qPCR or NanoString panel adapted from the 87-gene signature for FFPE tissue) with pre-specified cut-offs; (ii) prospectively validate its incremental value beyond standard clinicopathologic factors (AJCC stage, grade, age, and treatment) using calibration and decision-curve analyses; and (iii) use the P-high status to enrich early-phase testing of nominated vulnerabilities (CDC37–HSP90, PI3K/MAPK, and lipid-metabolism inhibitors) in patient-derived organoids/PDXs and, ultimately, biomarker-stratified trials. Given the immunosuppressive, hypoxia-linked microenvironment of P-high tumours, rational combinations with standard chemotherapy or immunotherapy should also be explored, while carefully monitoring potential on-target toxicities of palmitoylation-pathway modulation.

Limitations include the retrospective nature of the cohorts and the lack of direct biochemical validation of palmitoylated proteins; prospective trials and acyl-biotin exchange or mass-spectrometry studies are now warranted. Nevertheless, our work positions palmitoylation as a central, targetable node that rewires the gastric-cancer ecosystem at single-cell resolution. Targeting this lipid switch—either directly through DHHC/depalmitoylase inhibitors or indirectly via CDC37-HSP90 and PI3K-MAPK blockade—offers a rational strategy to dismantle the multicellular network driving metastasis and to deliver precision prognosis for patients with advanced GC.

Palmitoylation is associated with a multicellular, pro-metastatic gastric-cancer ecosystem that transcends individual cell lineages. A single-cell-derived, 87-gene palmitoylation-risk signature robustly stratifies patient survival and exposes druggable CDC37–HSP90 and PI3K/MAPK vulnerabilities. Consequently, quantifying or therapeutically targeting palmitoylation programmes offers an potentially translatable route for precision prognosis and treatment in GC; however, prospective validation and implementation studies (assay standardisation, cut-off definition, and clinical decision impact) will be required before routine use. Looking ahead, these findings may motivate noninvasive diagnostic tools—such as palmitoylation-sensitive imaging probes and plasma-based biomarkers (e.g., circulating or exosome-associated palmitoylation-related transcripts/proteins)—to support risk stratification and longitudinal disease monitoring in GC.

Methods

Transcriptomic data acquisition and pre-processing

RNA-seq profiles and matched clinical data for 350 GC samples were retrieved from The Cancer Genome Atlas (TCGA) and converted to TPM, followed by log2 transformation. Five GEO microarray series (GSE15459, $n = 192$; GSE15460, $n = 248$; GSE57303, $n = 70$; GSE62254, $n = 300$; GSE84437, $n = 433$) were merged, normalised with limma::normalizeBetweenArrays and batch-corrected using the empirical Bayes ComBat algorithm (sva), with the originating study as the batch variable. The pooled GEO cohort was split 7:3 into training and validation sets.

Single-cell and spatial transcriptomic data

ScRNA-seq data were downloaded from GSE167297 (ten tumours), GSE184198 (1 tumour) and OMIX001073 (14 tumours), yielding 119 931 cells from 25 samples. Analyses were performed with Seurat (v4.1.3) in R (v4.1.3). Count matrices were generated against the human reference genome GRCh38 (hg38), as reported in the original studies. Quality control excluded cells with >20% mitochondrial reads, >3% haemoglobin counts, <200 or >25 000 UMIs, or <200 or >8 000 detected genes. After QC, data were normalised and scaled, and cell-cycle effects (S.Score and G2M.Score) were regressed out. The top 2000 variable features were identified, and batch effects across samples/studies were mitigated using Harmony integration within Seurat. Dimensionality reduction was performed by PCA, and the top 30 PCs were used for neighbour graph construction, UMAP embedding and Louvain clustering (resolution 0.8). A fixed random seed (set.seed = 1234) was used for stochastic steps (e.g., UMAP initialisation) to ensure reproducibility. Differentially expressed marker genes were identified with FindAllMarkers ($p < 0.05$; $|\log2FC| > 0.25$; min.pct > 0.1).

Spatial transcriptomes (10 GC sections, GSE251950) were processed with SpaceRanger (10x Genomics) using the GRCh38 reference, followed by SCTransform. Median spot number was 3 229 (9886 UMIs, 3373 genes, 2% mitochondrial reads). Cell-type deconvolution of spots was performed with CARD using the scRNA-seq reference.

Palmitoylation-state calling in single cells

A literature-curated signature of 187 palmitoylation-associated genes (PAGs) was integrated into the CHPF framework to compute per-cell palmitoylation scores using ridge-penalised regression ($\lambda = 0.032$). Briefly, ridge regression learns a stable coefficient for each PAG and defines the palmitoylation score as a regularised, coefficient-weighted sum of normalised expression values, thereby reducing the impact of collinearity and dropouts in scRNA-seq data. The penalty parameter λ was selected by k-fold cross-validation (as implemented in CHPF) to minimise cross-validated reconstruction error while maintaining coefficient stability, and the optimal value ($\lambda = 0.032$) was fixed for all downstream analyses. Malignant epithelial cells (EPCAM+ epithelial cells with inferCNV/CopyKAT-defined high CNV/aneuploidy) with scores >2.5 were classified as Palmitoylation-high (P-high), those ≤2.5 as Palmitoylation-low (P-low). The cut-off of 2.5 was determined in the GEO training cohort by scanning candidate thresholds and selecting the value that maximised overall-survival separation (log-rank statistic); biologically, this stringent threshold captures an extreme high-score tail enriched for core palmitoylation regulators and palmitoylation-related pathways, such that "P-high" represents a transcriptionally palmitoylation-activated state rather than a direct biochemical readout. The threshold was then locked and applied unchanged across all validation sets.

Gene selection for the palmitoylation-associated gene set. To build the 187-gene palmitoylation-associated gene (PAG) panel, we combined evidence from curated databases and experimental studies. First, all human S-palmitoylation "writers" (ZDHHC palmitoyltransferases) and established "erasers" (depalmitoylases/thioesterases, including LYPLA1/2, ABHD17A/B/C and PPT1/2) were collected based on UniProtKB and Gene Ontology annotations related to protein S-palmitoylation and thioester hydrolysis. Second, we retrieved human proteins reported to be S-palmitoylated from public palmitoyl-proteome/PTM resources (e.g., SwissPalm and dbPTM) and retained only entries supported by direct experimental evidence (such as acyl-biotin exchange/acyl-RAC, metabolic labelling with palmitate analogues, or mass spectrometry). Third, cancer-relevant palmitoylation regulators and substrates were supplemented through manual literature curation. After merging sources, we removed duplicates, harmonised gene symbols to HGNC, and excluded low-confidence entries, resulting in a non-redundant 187-gene PAG panel used for CHPF scoring.

To clarify the biological scope of this palmitoylation gene set, we annotated the 187 PAGs into three functional tiers: (i) writers, i.e., DHHC palmitoyltransferases (ZDHHC family) that catalyse S-palmitoylation; (ii) erasers, i.e., depalmitoylases/thioesterases (e.g., LYPLA1/2, ABHD17A/B/C, and PPT1/2) that remove thioester-linked palmitate; and (iii) readers/

effectors, operationally defined as palmitoylation-dependent adaptors/trafficking components and experimentally supported palmitoylated substrates. Importantly, the CHPF ridge model does not impose category-specific weights; gene coefficients are learned from the data, such that the palmitoylation score reflects the integrated transcriptional activity of the palmitoylation cycle rather than being biased toward a single class of regulators.

Cell annotation

Lineage markers: epithelial (EPCAM, KRT18, KRT19, CDH1), fibroblast (DCN, THY1, COL1A1, COL1A2), endothelial (PECAM1, CLDN2, FLT1, RAMP2), T cell (CD3D/E/G, TRAC), NK cell (NKG7, GNLY, NCAM1, KLRD1), B cell (CD79A, IGHM, IGHG3, IGHA2), plasma cell (JCHAIN), myeloid (LYZ, MARCO, CD68, FCGR3A) and mast cell (KIT, MS4A2, GATA2). Malignant epithelial subsets were re-clustered to explore intra-tumour heterogeneity.

Weighted gene co-expression network analysis (WGCNA) and enrichment

WGCNA was applied to identify gene modules associated with P-high cells. Module eigengenes were tested for correlation with palmitoylation status. GO-BP and KEGG enrichment were performed with clusterProfiler.

Cell–cell communication

CellChat was used to infer ligand–receptor interactions among P-high, P-low and stromal/immune subsets. Communication probabilities were computed and aggregated into interaction networks.

Copy-number inference

InferCNV and CopyKAT were run on epithelial cells using endothelial and fibroblast cells as diploid references. Epithelial cells were classified as malignant when they displayed broad CNV deviations in inferCNV and were called aneuploid by CopyKAT; cells with near-flat inferCNV profiles and CopyKAT diploid ("normal") calls were labelled benign. Clusters enriched for benign/diploid cells were excluded from downstream malignant-epithelial analyses.

Transcription-factor (TF) activity

SCENIC was employed to reconstruct regulons active in P-high versus P-low cells. GRNBoost2 identified co-expression modules; top 1% TFs by degree were retained for downstream modelling.

Prognostic model construction

Univariate Cox regression screened P-high-specific TFs and target genes for overall survival association in TCGA ($p < 0.05$). Significant hits were entered into a machine-learning ensemble comprising 10 survival algorithms (RSF, Enet, Lasso, Ridge, stepwise Cox, CoxBoost, plsRcox, SuperPC, GBM and survival-SVM) and 101 algorithmic combinations.

Model hyperparameters were tuned using an inner 5-fold cross-validation, and predictive performance was estimated using an outer 10-fold cross-validation repeated 100 times. A fixed random seed (set.seed = 1234) was used for all resampling and model training steps. The best-performing model was locked and tested in the merged GEO cohorts without refitting. Detailed data harmonisation, leakage control and the full nested cross-validation procedure are described below.

Survival-model validation and nested cross-validation

The TCGA-STAD cohort was used as the discovery and training dataset, while five GEO microarray datasets (GSE15459, GSE15460, GSE57303, GSE62254, and GSE84437) served as independent external validation sets. Bulk transcriptomic data acquisition and pre-processing are described in Materials and Methods ("Transcriptomic data acquisition and pre-processing"). Survival data were harmonised by transforming overall survival times into consistent units. Candidate prognostic features consisted of TFs and downstream genes specifically enriched in the P-high subtype identified from single-cell analysis.

Univariate Cox regression was first performed to screen features associated with overall survival ($p < 0.05$), followed by removal of highly correlated genes ($|\text{Spearman } \rho| \geq 0.85$). The selected features were used to train a comprehensive ensemble of 101 machine-learning models encompassing ten algorithmic families, including random survival forest (RSF), elastic-net Cox (Enet), Lasso-Cox, Ridge-Cox, stepwise Cox, CoxBoost, partial least squares Cox (plsRcox), SuperPC, gradient boosting machine (GBM), and survival-SVM. Model construction and evaluation were conducted in R (4.1.3) using corresponding packages (randomForestSRC, glmnet, CoxBoost, gbm, survivalsvm, etc.). Nested cross-validation (inner 5-fold CV for hyperparameter tuning, outer 10-fold CV repeated 100 times) was applied to estimate unbiased predictive performance, measured by Harrell's C-index.

The optimal model, identified by the highest mean C-index in the TCGA training set, was locked and validated in each GEO cohort without re-fitting. Prognostic risk scores were computed using the linear predictor from the final Ridge-Cox model ($\lambda = 0.032$), and a cut-off value determined in TCGA via maximally selected rank statistics was applied consistently across validation sets. Model robustness was further evaluated by time-dependent ROC, calibration, and decision-curve analyses. This framework ensured transparent separation between model training and validation, thereby addressing reproducibility and generalisability of the 101-algorithm machine-learning signature.

Somatic alterations

GISTIC2.0 delineated focal CNVs; maftools calculated tumour mutational burden (TMB).

Functional Validation Experiments for SH3BGRL

To functionally validate SH3BGRL, a candidate gene highlighted by the prognostic model, we performed the following in silico, in vitro and in vivo assays.

SH3BGRL expression analysis in TCGA. RNA-sequencing data (FPKM format) and corresponding clinical information for stomach adenocarcinoma (STAD) were downloaded from The Cancer Genome Atlas (TCGA) portal. SH3BGRL expression levels between gastric tumour tissues and matched normal adjacent tissues were compared using an unpaired two-tailed Student's t-test. For survival analysis, patients were stratified into SH3BGRL high- and low-expression groups based on the optimal cut-off value determined by the 'surv_cutpoint' function from the R 'survminer' package. Kaplan-Meier survival curves were plotted, and the log-rank test was used to assess statistical significance.

Cell Culture and Lines. The immortalised human gastric mucosal epithelial cell line GES-1 and the human GC cell lines (AGS, BGC823, NCI-N87, HGC-27) were obtained from the Procell (Wuhan, China). All cell lines were cultured in RPMI-1640 medium (Gibco), supplemented with 10% foetal bovine serum (FBS, Gibco) and 1% penicillin-streptomycin (Gibco), at 37 °C in a humidified incubator with 5% CO_2.

Plasmid Construction and Cell Line Engineering. For knockdown experiments, two specific short hairpin RNA (shRNA) sequences targeting human SH3BGRL and a non-targeting control (shNC) were cloned into the pLKO.1-puro vector. For overexpression, the full-length coding sequence of human SH3BGRL was amplified and cloned into the LV5-puro lentiviral vector (GenePharma). An empty vector was used as the negative control (Vector). Lentiviruses were produced in 293 T cells using the psPAX2 and pMD2.G packaging plasmids. BGC823 and AGS cells were transduced with the respective viruses and selected with 2 μg/mL puromycin for 10 days to generate stable cell lines.

Quantitative Real-Time PCR (qRT–PCR). Total RNA was extracted from cells using TRIzol reagent (Invitrogen). cDNA was synthesised using the PrimeScript RT reagent Kit (Takara). qRT–PCR was performed on a QuantStudio 5 Real-Time PCR System (Applied Biosystems) using SYBR

Green Premix Pro Taq HS (Accurate Biology). Gene expression was normalised to GAPDH and calculated using the 2^(-ΔΔCt) method.

Cell Proliferation and Colony Formation Assays. Cell proliferation was assessed using the Cell Counting Kit-8 (CCK-8, Dojindo) according to the manufacturer's instructions. Briefly, 2000 cells per well were seeded in a 96-well plate. At 24, 48, and 72 h, 10 μL of CCK-8 reagent was added to each well, followed by incubation for 2 h. The absorbance at 450 nm was measured using a microplate reader. For the colony formation assay, 1000 cells were seeded into each well of a 6-well plate and cultured for 10-14 days. The resulting colonies were fixed with 4% paraformaldehyde, stained with 0.1% crystal violet, and manually counted.

Apoptosis Analysis by Flow Cytometry. Cell apoptosis was detected using an Annexin V-FITC/PI Apoptosis Detection Kit (BD Biosciences). Briefly, 1 × 10^5 cells were collected, washed with cold PBS, and resuspended in 100 μL of 1× Binding Buffer. The cells were then stained with 5 μL of Annexin V-FITC and 5 μL of Propidium Iodide (PI) for 15 min in the dark at room temperature. Subsequently, 400 μL of 1× Binding Buffer was added, and the samples were analysed immediately using a flow cytometer (BD Accuri C6). The data were analysed using FlowJo software.

Cell Invasion and Migration Assays. Cell invasion and migration abilities were evaluated using 24-well Transwell chambers (8-μm pore size, Corning). For the invasion assay, the upper chambers were pre-coated with Matrigel (BD Biosciences). For the migration assay, chambers were left uncoated. A total of 5 × 10^4 cells in 200 μL of serum-free medium were seeded into the upper chamber. The lower chamber was filled with 600 μL of complete medium containing 20% FBS as a chemoattractant. After 24–48 h of incubation, the cells that had traversed the membrane were fixed with 4% paraformaldehyde, stained with 0.1% crystal violet, and photographed and counted under a microscope in five random fields.

Western Blot Analysis. Total proteins were extracted from cells using RIPA lysis buffer (Beyotime) containing protease and phosphatase inhibitors. Protein concentrations were determined using a BCA protein assay kit (Beyotime). Equal amounts of protein (20–30 μg) were separated by 10% SDS-PAGE and transferred onto PVDF membranes (Millipore). The membranes were blocked with 5% non-fat milk and then incubated overnight at 4 °C with primary antibodies against: SH3BGRL (1:1000, Proteintech, Cat#11253-1-AP), E-cadherin (1:1000, Proteintech, Cat#20874-1-AP), Vimentin (1:1000, Proteintech, Cat#10366-1-AP), and GAPDH (1:5000, Proteintech, Cat#60004-1-Ig). After washing, the membranes were incubated with HRP-conjugated secondary antibodies for 1 h at room temperature. Protein bands were visualised using an ECL detection kit (Millipore) and imaged with a chemiluminescence imaging system.

Mouse Xenograft Model. Six-week-old male NOD-scid mice were purchased from Vital River Laboratory (Beijing, China) and housed under specific pathogen-free conditions. All animal experiments were approved by the Institutional Animal Care and Use Committee of China Pharmaceutical University. For the subcutaneous xenograft model, 5 × 10^6 BGC823#shNC or BGC823#shSH3BGRL cells in 100 μL of PBS mixed with Matrigel (1:1) were injected into the right flanks of the mice ($n = 5$ per group). Tumour dimensions were measured with calipers every 3 days, and tumor volume was calculated using the formula: Volume = (Length × Width^2)/2. On day 20 post-inoculation, mice were deeply anaesthetised and euthanized by intraperitoneal injection of 1.25% tribromoethanol (20 mL/kg). Adequate anaesthesia (unconsciousness) was confirmed by loss of the righting reflex and absence of the pedal withdrawal reflex to minimise pain and distress during terminal tissue collection; tumours were then dissected, excised, weighed, and processed for subsequent analyses.

Immunohistochemistry (IHC) and TUNEL Staining. Resected tumor tissues were fixed in 4% paraformaldehyde, embedded in paraffin, and sectioned at 4-μm thickness. For IHC, sections were deparaffinized, rehydrated, and subjected to antigen retrieval. Endogenous peroxidase activity was blocked with 3% H_2O_2. The sections were then blocked and incubated overnight at 4 °C with an anti-Ki-67 antibody (1:500, Proteintech, Cat#27309-1-AP). After incubation with a secondary antibody, the signal was developed with DAB substrate and counterstained with hematoxylin.

Apoptosis in tumor sections was detected using a TUNEL assay kit (Roche) according to the manufacturer's instructions. The stained sections were imaged under a light microscope.

Statistical analysis

All analyses were performed in R (v4.1.3). Continuous variables were compared using the Wilcoxon rank-sum test or Student's t-test, as appropriate, and categorical variables were compared using chi-square tests. Correlation was assessed by Pearson's r. Survival analyses used Kaplan–Meier curves with log-rank tests and multivariable Cox proportional hazards regression. P values were two-sided unless otherwise specified. For analyses involving multiple hypotheses (including differential expression and functional enrichment), false discovery rate (FDR) was controlled using the Benjamini–Hochberg procedure. Survival associations reported as hazard ratios were estimated using Cox proportional hazards models; multivariable models adjusted for age and AJCC pathological stage, and additionally for chemotherapy/radiotherapy when such TCGA.

Data Availability

The datasets generated and/or analysed during the current study are available in the corresponding repositories. RNA sequencing data and associated clinical data for GC samples were retrieved from The Cancer Genome Atlas (TCGA) and can be accessed through the TCGA portal. Single-cell RNA-seq and spatial transcriptomics data are available from the GEO database (accession numbers: GSE167297, GSE184198, OMIX001073). Further inquiries regarding the datasets should be directed to the corresponding authors.

Received: 27 October 2025; Accepted: 24 February 2026;
Published online: 07 March 2026

References

1. Sundar, R. et al. Gastric cancer. *Lancet* **405**, 2087–2102 (2025).
2. Duan, Y. et al. Helicobacter pylori and gastric cancer: mechanisms and new perspectives. *J. Hematol. Oncol.* **18**, 10 (2025).
3. Chen, Y. et al. Identification of core immune-related genes CTSK, C3, and IFITM1 for diagnosing Helicobacter pylori infection-associated gastric cancer through transcriptomic analysis. *Int J. Biol. Macromol.* **287**, 138645 (2025).
4. Wu, L. W. et al. Diffuse gastric cancer: a comprehensive review of molecular features and emerging therapeutics. *Target Oncol.* **19**, 845–865 (2024).
5. Chen, Y. et al. The current landscape of gastric cancer and gastroesophageal junction cancer diagnosis and treatment in China: a comprehensive nationwide cohort analysis. *J. Hematol. Oncol.* **18**, 42 (2025).
6. Ford, A. C. et al. Eradication therapy to prevent gastric cancer in helicobacterpylori-positive individuals: systematic review and meta-analysis of randomized controlled trials and observational studies. *Gastroenterology* **169**, 261–276 (2025).
7. Liu, Y. et al. Traditional Chinese medicine in the treatment of chronic atrophic gastritis, precancerous lesions and gastric cancer. *J. Ethnopharmacol.* **337**, 118812 (2025).
8. Pei, L. et al. Electroacupuncture reduces duration of postoperative ileus after laparoscopic gastrectomy for gastric cancer: a multicenter randomized trial. *Gastroenterology* **169**, 73–84 (2025).
9. Shah, S. C. et al. AGA clinical practice update on screening and surveillance in individuals at increased risk for gastric cancer in the united states: expert review. *Gastroenterology* **168**, 405–416.e1 (2025).
10. Ren, L. et al. Effectiveness of the CANCER-AIMS intervention on nutritional status and symptom management in patients with gastric cancer following gastrectomy: a randomized controlled trial. *Int J. Nurs. Stud.* **159**, 104873 (2024).

11. Yu, H. et al. Alkannin triggered apoptosis and ferroptosis in gastric cancer by suppressing lipid metabolism mediated by the c-Fos/SREBF1 axis. *Phytomedicine* **140**, 156604 (2025).
12. Shoji, H. et al. Phosphoproteomic subtyping of gastric cancer reveals dynamic transformation with chemotherapy and guides targeted cancer treatment. *Cell Rep.* **43**, 114774 (2024).
13. Hwang, K. et al. Targeted degradation of METTL3 against acute myeloid leukemia and gastric cancer. *Eur. J. Med Chem.* **279**, 116843 (2024).
14. Jiang, X. et al. Eleutheroside A inhibits PI3K/AKT1/mTOR-mediated glycolysis in MDSCs to alleviate their immunosuppressive function in gastric cancer. *Int Immunopharmacol.* **159**, 114907 (2025).
15. Zhao, Z. et al. Helicobacter pylori activates SLFN4(+)MDSCs to accelerate gastric intestinal metaplasia. *iScience* **27**, 111255 (2024).
16. Shen, Y., et al. Rg3-lipo biomimetic delivery of paclitaxel enhances targeting of tumors and myeloid-derived suppressor cells. *J. Clin. Invest.* **134**, e178617 (2024).
17. Mo, Y. et al. ZDHHC20 mediated S-palmitoylation of fatty acid synthase (FASN) promotes hepatocarcinogenesis. *Mol. Cancer* **23**, 274 (2024).
18. Chaturvedi, S. & Sonawane, A. Recapitulating the potential contribution of protein S-palmitoylation in cancer. *Cancer Metastasis Rev.* **44**, 20 (2024).
19. Natale, F. et al. Inhibition of zDHHC7-driven protein S-palmitoylation prevents cognitive deficits in an experimental model of Alzheimer's disease. *Proc. Natl. Acad. Sci. USA* **121**, e2402604121 (2024).
20. Wei, F. et al. ZDHHC7-mediated S-palmitoylation of ATG16L1 facilitates LC3 lipidation and autophagosome formation. *Autophagy* **20**, 2719–2737 (2024).
21. Huang, B. et al. Palmitoylation-dependent regulation of GPX4 suppresses ferroptosis. *Nat. Commun.* **16**, 867 (2025).
22. Zheng, W. et al. S-palmitoylation modulates ATG2-dependent non-vesicular lipid transport during starvation-induced autophagy. *Embo J.* **44**, 2596–2619 (2025).
23. Xin, L. et al. Methionine Restriction Exerts Anti-Tumor Immunity via Joint Intervention of T-Bet palmitoylation in gastric cancer. *Biotechnol. J.* **20**, e202400574 (2025).
24. Liu, S. et al. Helicobacter pylori CagA promotes gastric cancer immune escape by upregulating SQLE. *Cell Death Dis.* **16**, 17 (2025).
25. Xu, M. et al. Palmitoyltransferase ZDHHC3 aggravates nonalcoholic steatohepatitis by targeting s-palmitoylated IRHOM2. *Adv. Sci.* **10**, e2302130 (2023).
26. Tang, F. et al. A pan-cancer single-cell panorama of human natural killer cells. *Cell* **186**, 4235–4251 (2023).
27. Mahat, D. B. et al. Single-cell nascent RNA sequencing unveils coordinated global transcription. *Nature* **631**, 216–223 (2024).
28. Ma, L. et al. Single-cell RNA-seq reveals novel interaction between muscle satellite cells and fibro-adipogenic progenitors mediated with FGF7 signalling. *J. Cachexia Sarcopenia Muscle* **15**, 1388–1403 (2024).
29. Jiang, H. et al. Revealing the transcriptional heterogeneity of organ-specific metastasis in human gastric cancer using single-cell RNA Sequencing. *Clin. Transl. Med.* **12**, e730 (2022).
30. Zhai, Y. et al. Single-cell RNA sequencing integrated with bulk RNA sequencing analysis reveals diagnostic and prognostic signatures and immunoinfiltration in gastric cancer. *Comput. Biol. Med.* **163**, 107239 (2023).
31. Wang, Z. et al. Identifying mitophagy-related genes as prognostic biomarkers and therapeutic targets of gastric carcinoma by integrated analysis of single-cell and bulk-RNA sequencing data. *Comput. Biol. Med.* **163**, 107227 (2023).
32. Kuppe, C. et al. Spatial multi-omic map of human myocardial infarction. *Nature* **608**, 766–777 (2022).
33. Li, J., Wu, Z., and Lin, R. Impact of Helicobacter pylori on immunotherapy in gastric cancer. *J. Immunother. Cancer* **12**, e010354 (2024).
34. Kim, H. D. et al. Survival outcomes of patients with gastric cancer treated with first-line nivolumab plus chemotherapy based on claudin 18.2 expression. *Gastric Cancer* **28**, 74–82 (2025).
35. Kumar, V. et al. Single-cell atlas of lineage states, tumor microenvironment, and subtype-specific expression programs in gastric cancer. *Cancer Discov.* **12**, 670–691 (2022).
36. Ko, P. J. & Dixon, S. J. Protein palmitoylation and cancer. *EMBO Rep.* **19**, e46666 (2018).
37. Yao, H. et al. Inhibiting PD-L1 palmitoylation enhances T-cell immune responses against tumours. *Nat. Biomed. Eng.* **3**, 306–317 (2019).
38. Shen, Z. H. et al. Unveiling the role of protein palmitoylation in gastric cancer diagnosis via machine learning. *Discov. Oncol.* **16**, 1982 (2025).
39. Zhang, Z. et al. Palmitoylation of TIM-3 promotes immune exhaustion and restrains antitumor immunity. *Sci. Immunol.* **9**, eadp7302 (2024).
40. He, Y. et al. Palmitic acid accelerates endothelial cell injury and cardiovascular dysfunction via palmitoylation of PKM2. *Adv. Sci.* **12**, e2412895 (2025).
41. Rocks, O. et al. An acylation cycle regulates localization and activity of palmitoylated Ras isoforms. *Science* **307**, 1746–1752 (2005).
42. Plowman, S. J. et al. H-ras, K-ras, and inner plasma membrane raft proteins operate in nanoclusters with differential dependence on the actin cytoskeleton. *Proc. Natl. Acad. Sci. USA* **102**, 15500–15505 (2005).
43. Runkle, K. B. et al. Inhibition of DHHC20-mediated EGFR palmitoylation creates a dependence on EGFR signaling. *Mol. Cell* **62**, 385–396 (2016).
44. Zhang, Z. et al. Cardiolipin-mimic lipid nanoparticles without antibody modification delivered senolytic in vivo CAR-T therapy for inflamm-aging. *Cell Rep. Med.* **6**, 102209 (2025).
45. Papp, T. E. et al. CD47 peptide-cloaked lipid nanoparticles promote cell-specific mRNA delivery. *Mol. Ther.* **33**, 3195–3208 (2025).
46. Song, P. et al. Palmitic acid and palmitoylation in cancer: understanding, insights, and challenges. *Innovation* **6**, 100918 (2025).
47. Yang, K. et al. The role of lipid metabolic reprogramming in tumor microenvironment. *Theranostics* **13**, 1774–1808 (2023).

Acknowledgements

This study was supported by the General Programme of Health Commission of WuXi (No. M202330) and the collaborative custom development of RNA probes at Soochow University (No. P112213323). The authors would like to acknowledge the contributions of the research participants and the technical support from the institutions involved in this project.

Author contributions

J.X., Y.H., and Q.Q. contributed equally to this work. J.X. conceived and designed the study. Y.H. and Q.Q. performed data acquisition, preprocessing, and integration of the TCGA and GEO datasets. Y.D.L. and F.C. developed and optimised the machine-learning framework and conducted model training and validation. S.S.H. and H.B.Y. performed the single-cell and spatial transcriptomic analyses. J.L. supervised the computational experiments and provided methodological guidance. Y.Q. and S.H.X. coordinated the project, provided critical revisions, and secured funding. J.X., Y.H., and Q.Q. drafted the manuscript. Y.D.L., F.C., S.S.H., and H.B.Y. prepared figures and contributed to data visualisation. J.L., Y.Q., and S.H.X. reviewed and edited the manuscript. All authors discussed the results, approved the final version, and agree to be accountable for all aspects of the work.

Competing interests
The authors declare no competing interests.

Additional information
Supplementary information The online version contains supplementary material available at https://doi.org/10.1038/s41698-026-01359-4.

Correspondence and requests for materials should be addressed to Jian Lv , Yan Qin or Suhua Xia.

Reprints and permissions information is available at http://www.nature.com/reprints

Publisher's note Springer Nature remains neutral with regard to jurisdictional claims in published maps and institutional affiliations.

Open Access This article is licensed under a Creative Commons Attribution-NonCommercial-NoDerivatives 4.0 International License, which permits any non-commercial use, sharing, distribution and reproduction in any medium or format, as long as you give appropriate credit to the original author(s) and the source, provide a link to the Creative Commons licence, and indicate if you modified the licensed material. You do not have permission under this licence to share adapted material derived from this article or parts of it. The images or other third party material in this article are included in the article's Creative Commons licence, unless indicated otherwise in a credit line to the material. If material is not included in the article's Creative Commons licence and your intended use is not permitted by statutory regulation or exceeds the permitted use, you will need to obtain permission directly from the copyright holder. To view a copy of this licence, visit http://creativecommons.org/licenses/by-nc-nd/4.0/.

© The Author(s) 2026